

## RESEARCH ARTICLE

10.1002/2017JD026455

## Key Points:

- In the SoCAB, 20–36% of spatial variance in  $X_{\text{CO}_2}$  is explained by topography on scales  $\lesssim 10$  km
- In Pasadena,  $X_{\text{CO}_2}$  is enhanced by  $2.3 \pm 1.2$  ( $1\sigma$ ) ppm above background levels, at 1300 (UTC 8) with seasonal variation
- The SoCAB  $X_{\text{CO}_2}$  enhancement is in agreement for 3 different observation sets (TCCON, GOSAT, and OCO-2)

## Supporting Information:

- Supporting Information S1

## Correspondence to:

J. K. Hedelius and P. O. Wennberg,  
 jhedeliu@caltech.edu;  
 wennberg@caltech.edu

## Citation:

Hedelius, J. K., et al. (2017), Emissions and topographic effects on column  $\text{CO}_2$  ( $X_{\text{CO}_2}$ ) variations, with a focus on the Southern California Megacity, *J. Geophys. Res. Atmos.*, 122, 7200–7215, doi:10.1002/2017JD026455.

Received 4 JAN 2017

Accepted 5 JUN 2017

Accepted article online 6 JUN 2017

Published online 11 JUL 2017

## Emissions and topographic effects on column $\text{CO}_2$ ( $X_{\text{CO}_2}$ ) variations, with a focus on the Southern California Megacity

Jacob K. Hedelius<sup>1</sup> , Sha Feng<sup>2,3</sup>, Coleen M. Roehl<sup>4</sup>, Debra Wunch<sup>5</sup> , Patrick W. Hillyard<sup>6,7</sup>, James R. Podolske<sup>6</sup>, Laura T. Iraci<sup>6</sup> , Risa Patarasuk<sup>8</sup> , Preeti Rao<sup>2,9</sup> , Darragh O'Keefe<sup>8</sup>, Kevin R. Gurney<sup>8</sup> , Thomas Lauvaux<sup>2,3</sup>, and Paul O. Wennberg<sup>4,10</sup> 

<sup>1</sup>Division of Chemistry and Chemical Engineering, California Institute of Technology, Pasadena, CA, USA, <sup>2</sup>Jet Propulsion Laboratory, California Institute of Technology, Pasadena, California, USA, <sup>3</sup>Department of Meteorology and Atmospheric Science, Pennsylvania State University, University Park, Pennsylvania, USA, <sup>4</sup>Division of Geological and Planetary Sciences, California Institute of Technology, Pasadena, California, USA, <sup>5</sup>Department of Physics, University of Toronto, Toronto, Ontario, Canada, <sup>6</sup>NASA Ames Research Center, Mountain View, California, USA, <sup>7</sup>Bay Area Environmental Research Institute, Petaluma, California, USA, <sup>8</sup>School of Life Science, Arizona State University, Tempe, Arizona, USA, <sup>9</sup>School of Natural Resources and Environment, University of Michigan, Ann Arbor, Michigan, USA, <sup>10</sup>Division of Engineering and Applied Science, California Institute of Technology, Pasadena, California,

**Abstract** Within the California South Coast Air Basin (SoCAB),  $X_{\text{CO}_2}$  varies significantly due to atmospheric dynamics and the nonuniform distribution of sources.  $X_{\text{CO}_2}$  measurements within the basin have seasonal variation compared to the “background” due primarily to dynamics, or the origins of air masses coming into the basin. We observe basin-background differences that are in close agreement for three observing systems: Total Carbon Column Observing Network (TCCON)  $2.3 \pm 1.2$  ppm, Orbiting Carbon Observatory-2 (OCO-2)  $2.4 \pm 1.5$  ppm, and Greenhouse gases Observing Satellite  $2.4 \pm 1.6$  ppm (errors are  $1\sigma$ ). We further observe persistent significant differences ( $\sim 0.9$  ppm) in  $X_{\text{CO}_2}$  between two TCCON sites located only 9 km apart within the SoCAB. We estimate that 20% ( $\pm 1\sigma$  confidence interval (CI): 0%, 58%) of the variance is explained by a difference in elevation using a full physics and emissions model and 36% ( $\pm 1\sigma$  CI: 10%, 101%) using a simple, fixed mixed layer model. This effect arises in the presence of a sharp gradient in any species (here we focus on  $\text{CO}_2$ ) between the mixed layer (ML) and free troposphere. Column differences between nearby locations arise when the change in elevation is greater than the change in ML height. This affects the fraction of atmosphere that is in the ML above each site. We show that such topographic effects produce significant variation in  $X_{\text{CO}_2}$  across the SoCAB as well.

**Plain Language Summary** Cities persistently have elevated carbon dioxide ( $\text{CO}_2$ ) levels as compared to surrounding regions. Within a city  $\text{CO}_2$  levels can also vary significantly at different locations for reasons such as more  $\text{CO}_2$  being emitted in some parts than others. Elevated column  $\text{CO}_2$  levels in the South Coast Air Basin (SoCAB) are in agreement for three observation systems (two satellite and one ground-based) systems and vary with regional wind patterns throughout the year. In Pasadena, California, within the SoCAB, a significant fraction (about 25%) of variation in the column-averaged  $\text{CO}_2$  can be explained by differences in surface altitude. This is important to understand so that all variations in column  $\text{CO}_2$  within an urban region are not mistakenly interpreted as being from  $\text{CO}_2$  surface fluxes.

### 1. Introduction

Carbon dioxide ( $\text{CO}_2$ ) is the single most important human influenced (anthropogenic) greenhouse gas (GHG) [Myhre et al., 2013]. Atmospheric  $\text{CO}_2$  concentrations have increased from  $278 \pm 2$  ppm in 1750 [Etheridge et al., 1996] to more than 400 ppm today (<https://www.esrl.noaa.gov/gmd/ccgg/trends/global.html>). The change in radiative forcing over the industrial era for all well-mixed anthropogenic greenhouse gases is  $2.83 \pm 0.29$   $\text{W m}^{-2}$ , and the change in  $\text{CO}_2$  alone accounts for  $1.82 \pm 0.19$   $\text{W m}^{-2}$  [Myhre et al., 2013]. Changes in radiative forcing due to  $\text{CO}_2$  increases have been directly observed [Feldman et al., 2015].

A significant fraction of anthropogenic  $\text{CO}_2$  emissions is a result of activities within urban areas. Central estimates of  $\text{CO}_2$  emissions related with urban final energy use are 76% globally and 86% of the total emissions in

North America [Seto *et al.*, 2014]. Because some CO<sub>2</sub> emissions related with urban use are from outside urban areas (e.g., due to imported electricity), primary or direct CO<sub>2</sub> emissions from urban areas are lower (30–56%, central estimate 43%). These fractions are somewhat disproportionate as urban areas house 54% of the world's population [United Nations, 2014] and cover only ~0.5% of ice-free terrestrial land [Schneider *et al.*, 2009].

Large urban agglomerations, or megacities, are particularly large anthropogenic emitters, with the 50 largest cities globally emitting more CO<sub>2</sub> equivalent than any country besides the United States and China [Hoornweg *et al.*, 2010]. One of these megacities is the greater Los Angeles (LA) area which fills much of the South Coast Air Basin (SoCAB) in California. The SoCAB has ~17 million inhabitants sprawled over four counties (Los Angeles, Orange, San Bernardino, and Riverside) and more than 160 cities. SoCAB emissions have been estimated to be on order of 167 Tg CO<sub>2</sub> yr<sup>-1</sup> [Wunch *et al.*, 2016] which is ~3.2% of fossil fuel and cement production CO<sub>2</sub> emissions from the United States or approximately 0.4% of the total global anthropogenic CO<sub>2</sub> emissions.

The SoCAB is a favorable test bed location for quantifying CO<sub>2</sub> emissions by remote sensing because of the unique wealth of available data. Los Angeles was chosen as one of two cities (besides Paris) in a pilot program to study megacity emissions [Duren and Miller, 2012]; Sao Paulo, Brazil, has since been chosen as a third city (<https://megacities.jpl.nasa.gov/portal/>). There have been several previous studies that have analyzed CO<sub>2</sub> activity within the SoCAB. Affek *et al.* [2007] used isotopic measurements of CO<sub>2</sub> from flask samples to analyze the seasonality and sources of air in Pasadena (~14 km NE of downtown LA). Newman *et al.* [2008, 2013, 2016] have studied CO<sub>2</sub> mixing ratios and isotopic composition since 1972 (primarily in Pasadena) and have used both isotopologues and air composition to partition sources of CO<sub>2</sub>. Djuricin *et al.* [2010] used isotope analysis on air samples collected ~58 km south of LA to apportion anthropogenic and biogenic CO<sub>2</sub> sources. Brioude *et al.* [2013] used aircraft measurements of CO<sub>2</sub> with the Weather Research and Forecasting Model (WRF) to estimate basin fluxes. Wunch *et al.* [2009] studied diurnal patterns of column-averaged CO<sub>2</sub> observed by ground-based remote sensing at a TCCON (Total Carbon Column Observing Network) site. Kort *et al.* [2012] studied the average column enhancement in the SoCAB using satellite observations. Feng *et al.* [2016] used a high-resolution (1.3 km) WRF model to study CO<sub>2</sub> patterns across the basin. Finally, Verhulst *et al.* [2016] described patterns of CO<sub>2</sub> variation observed using the SoCAB megacity tower network.

In addition to the atmospheric measurements of CO<sub>2</sub> just described, there are several detailed bottom up inventories that cover the SoCAB. Under California's Health and Safety Code (H and SC) 39607.4, the California Air Resources Board (CARB) is responsible to report California's GHG inventory. CARB combines various data sets on reported petroleum product use throughout the state to create GHG emission estimates. Other CO<sub>2</sub> emission products that cover the SoCAB are available, including the Hestia-LA Project™ by Arizona State University. The Hestia project quantifies fossil fuel CO<sub>2</sub> (FFCO<sub>2</sub>) emitting activity at the building and street level [Gurney *et al.*, 2012] and is the higher spatial-resolution successor to the Vulcan product for cities where it is available. A map of Hestia-LA v. 1.0 emissions is shown in Figure 1, along with maps of nightlights and topography.

The SoCAB is roughly 140 km × 50 km and is surrounded by mountains on three sides and the Pacific Ocean on the fourth. Prevailing midday winds at the surface are on-shore caused by the sea breeze and heated-slope mountain-valley flows, with return winds aloft [Shultz and Warner, 1981]. Typical wind speeds are maximum ~5–10 m s<sup>-1</sup>, which leads to polluted air accumulating in the north and eastern parts of the basin. Local pollution enhancements primarily stay in the mixed layer (ML), which is the layer of the atmosphere near the surface that responds to surface forcings on the timescale of about an hour or less (for a discussion of lidar ML measurements in Pasadena, see Ware *et al.* [2016]). Pollution continues to accumulate until the ML height increases enough, and the sea breeze front travels far enough for aged air to be pushed out over the mountains or vented through mountain passes. These effects cause CO<sub>2</sub> gradients within the basin, large diurnal changes of the column-averaged dry-air mole fraction (DMF) CO<sub>2</sub> ( $X_{\text{CO}_2}$ ) inland (2–8 ppm [Wunch *et al.*, 2009]), and consistent midday  $X_{\text{CO}_2}$  enhancements compared to the nearby rural desert region ( $3.2 \pm 1.5$  ( $1\sigma$ ) ppm [Kort *et al.*, 2012]). All of the enhancement in  $X_{\text{CO}_2}$  is expected to occur because of a CO<sub>2</sub> enhanced ML and is attributed almost completely to anthropogenic emissions [Kort *et al.*, 2013; Newman *et al.*, 2013].

Column-averaged DMFs (e.g.,  $X_{\text{CO}_2}$ ) have been suggested to be important tools for Measurement, Reporting, and Verifying (MRV) of emissions from urban areas [Kort *et al.*, 2012; McKain *et al.*, 2012; Keppel-Aleks *et al.*, 2013; Hase *et al.*, 2015; Wunch *et al.*, 2016].  $X_{\text{CO}_2}$  is measured long term with remote sensing instruments

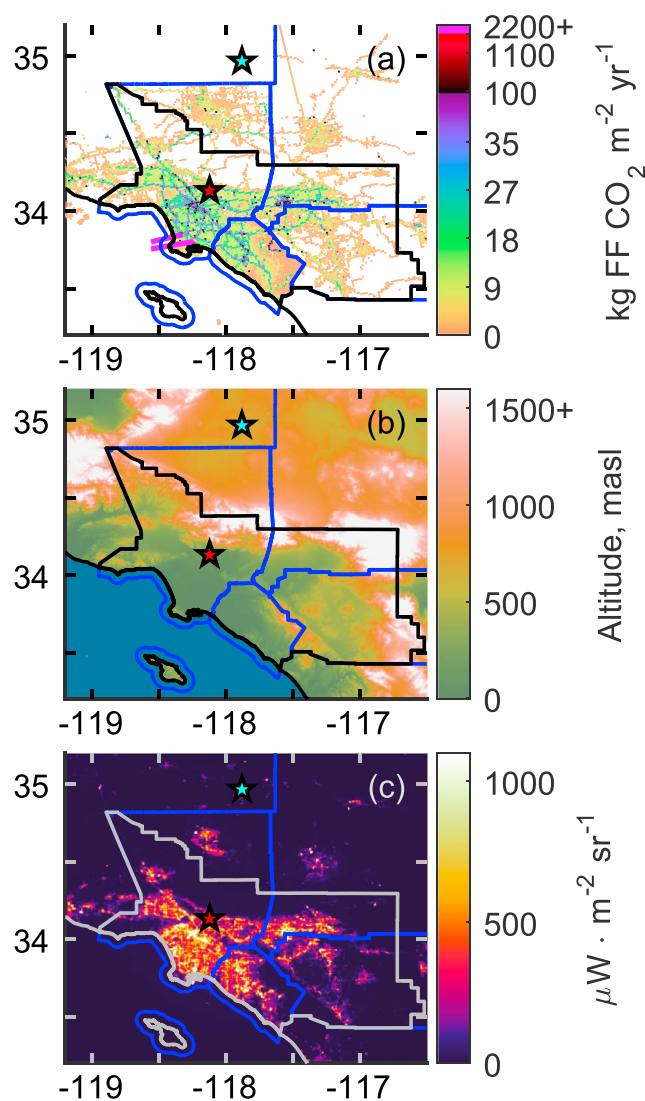


**Figure 1.** Maps of the SoCAB. The SoCAB boundary is shown in black (or gray). County boundaries are in blue. Red and cyan stars are for the Caltech and AFRC TCCON sites respectively. (a) Annually averaged gridded Hestia version 1.0, 2012 emissions. The two magenta lines are shown to draw the eye from the ocean to the two boxes with largest FFCO<sub>2</sub> emissions (2200+ kg m<sup>-2</sup> yr<sup>-1</sup>); otherwise, the boxes are too small to distinguish from surroundings. (b) Terrain of the area from the ASTER GDEM. (c) Nightlights intensities from January 2015 as measured by the Suomi NPP satellite.

tech and JPL. This is a ~0.28 mol m<sup>-2</sup> difference, or assuming an equal gradient along the full path between each sites 35 μmol m<sup>-2</sup> m<sup>-1</sup>. With a horizontal wind speed of 5 m s<sup>-1</sup> and no vertical mixing, this simple difference would require a 170 μmol CO<sub>2</sub> m<sup>-2</sup> s<sup>-1</sup> uptake or emission flux depending on wind direction—about 9 times the Hestia-LA flux at the Pasadena site [Feng et al., 2016] or about 7 times the largest diel gross ecosystem exchange from a temperate forest [Wehr et al., 2016].

If all of the difference is attributed to a surface flux in the example above, the result is unreasonably large. We explore other reasons for inner-basin X<sub>CO<sub>2</sub></sub> variance. In particular, we consider the effect of nonuniform weighting of the ML (e.g., by local topography changes) on X<sub>CO<sub>2</sub></sub> variations within the region due to a strong gradient between the ML and free troposphere. Here the strong gradient is from emissions, but variation due to topography could also occur in an area with high uptake, such as a productive forest. We evaluate whether

(e.g., by satellites or ground-based solar viewing spectrometers). It is defined as [Wunch et al., 2011]

$$X_{CO_2} = \frac{\text{column}_{CO_2}}{\text{column}_{\text{dry air}}} \quad (1)$$

Because X<sub>CO<sub>2</sub></sub> is dominated by the free troposphere, column measurements are less sensitive to local CO<sub>2</sub> concentrations than in situ measurements, but more sensitive to regional levels. Remote sensing of X<sub>CO<sub>2</sub></sub> from spaceborne instruments allows for observations where there are no ground-based X<sub>CO<sub>2</sub></sub> measurements.

MRV by column DMFs can be used to evaluate progress toward emission goals. Generally, emission goals are stated as percent decreases, so only relative (rather than absolute) changes in emissions over the observation period are needed. California, for example, has a goal to cut emissions to 1990 levels by 2020 and to 80% below 1990 levels by 2050 [Pavley and Nunez, 2006]. The city of Los Angeles has a goal to cut emissions to 35% below 1990 levels by 2030 [Villaraigosa, 2007]. In this study, we are interested in assessing the potential for using X<sub>CO<sub>2</sub></sub> for MRV in a city with well-studied emissions. In particular, we would like to understand contributions to X<sub>CO<sub>2</sub></sub> variations over small areas (a few kilometers), and across the basin.

Nonemissions related changes (e.g., from relative ML fractions) over small scales may be misinterpreted as a flux, which could bias results. This is important to recognize because X<sub>CO<sub>2</sub></sub> can vary significantly in the SoCAB. As an example, assume two sites 9 km apart have a consistent 0.9 ppm difference in X<sub>CO<sub>2</sub></sub>, and a surface pressure of about 980 hPa. This is approximately what the mean difference is between Cal-

$X_{\text{CO}_2}$  variability can be explained by different factors using models that include the underlying emissions and simulation of the atmospheric transport. We also determine how  $X_{\text{CO}_2}$  within the basin compares to nearby background levels.

In section 2 we describe the data sets and the models. In section 3 we examine how the  $X_{\text{CO}_2}$  enhancement within the basin has varied with time. In section 4 we describe reasons for  $X_{\text{CO}_2}$  variations within the SoCAB. We conclude in section 5 with our main findings.

## 2. Data Sets

We use three observational data sets (section 2.1–2.3) as well as three simulated  $X_{\text{CO}_2}$  products (section 2.4–2.5). These are described in more detail below.

### 2.1. TCCON

Ground-based measurements of  $X_{\text{CO}_2}$  were made at three TCCON sites [Wunch *et al.*, 2011]. The California Institute of Technology (Caltech) site in Pasadena, California (34.136°N, 118.127°W, 240 m above sea level (asl)), is located within the SoCAB. The Caltech site has been operational since September 2012 [Wennberg *et al.*, 2014b]. TCCON measurements at the Jet Propulsion Laboratory (JPL) were concurrent with Caltech TCCON measurements from January to June 2013 [Wennberg *et al.*, 2014a]. This site is also within the SoCAB (34.202°N, 118.175°W, 390 m asl) and less than 9 km from Caltech. In July 2013, the former JPL instrument was moved outside the SoCAB 95 km away to Armstrong Flight Research Center (AFRC) (34.960°N, 117.881°W, 700 m asl). This instrument has remained at AFRC since July 2013 [Iraci *et al.*, 2014]. Retrievals from the measurements at all three sites use the GGG2014 algorithm [Wunch *et al.*, 2015].

### 2.2. The Orbiting Carbon Observatory-2 (OCO-2), ACOS Version 7r

The OCO-2 satellite launched in 2014 [Eldering *et al.*, 2017]. Data from routine measurements are available from September 2014 onward. OCO-2  $X_{\text{CO}_2}$  measurements are tied to TCCON measurements [Wunch *et al.*, 2017], which are in turn tied to the World Meteorological Organization (WMO) standards [Wunch *et al.*, 2010]. The OCO-2 observations are tied to the TCCON by scaling observations at all sites across the globe rather than just the nearest ground site; thus, OCO-2 provides a separate and distinct set of  $X_{\text{CO}_2}$  from the TCCON that agrees on average globally. For this study we used data from the NASA Atmospheric CO<sub>2</sub> Observations from Space (ACOS) version 7r algorithm [Crisp *et al.*, 2012; O'Dell *et al.*, 2012]. OCO-2 measures  $X_{\text{CO}_2}$  globally at a resolution of about 1.3 km × 2.25 km, across eight longitudinal pixels. It is in a Sun-synchronous orbit and has an equatorial crossing time of around 1 P.M. local solar time. Worden *et al.* [2016] found typical land measurement precision (1 $\sigma$ ) and accuracy to be 0.75 ppm and 0.65 ppm with the caveat that the precision estimate includes effects of synoptic variability. We describe the filtering of OCO-2 data and “background” selection in Appendix A.

### 2.3. GOSAT-ACOS Version 7.3

The Greenhouse gases Observing Satellite (GOSAT) was developed by the Japan Aerospace Exploration Agency (JAXA) and measures thermal and near-IR spectra from which  $X_{\text{CO}_2}$  and  $X_{\text{CH}_4}$  can be retrieved [Kuze *et al.*, 2016]. GOSAT footprints are ~10.5 km in diameter [Kuze *et al.*, 2009]. The ACOS algorithm used for  $X_{\text{CO}_2}$  retrievals from OCO-2 has also been used to retrieve  $X_{\text{CO}_2}$  from GOSAT measurements. As of 2016, the latest version is 7.3 and uses the V201 radiance spectra [Kuze *et al.*, 2016]. Data from April 2009 to May 2016 were used in this study.

### 2.4. WRF Model with Hestia-LA

Hestia-LA estimates FFCO<sub>2</sub> emissions at the scale of buildings and street segments for the five counties associated with the SoCAB region [Gurney *et al.*, 2012]. The version 1.0 data product generated estimates for the 2010–2012 time period and was used in this study. (Version 2.0 is now available upon request to kevin.gurney@asu.edu. Version 2.0 covers the 2010–2015 time period). Hestia-LA is resolved temporally to the hourly scale, accounting for diurnal, weekly, and monthly differences. The average weekday to weekend emission ratio is ~1.23 (Figure 2) for the Hestia-LA product and dates used in this study. The version of Hestia used in this simulation does not include CO<sub>2</sub> emissions from nonfossil fuel sectors, which are estimated to be 19% of California's total CO<sub>2</sub> emissions [Hanemann *et al.*, 2008].

Hestia-LA was coupled with a 50 layer, 1.3 km × 1.3 km WRF simulation described in more detail by Feng *et al.* [2016]. The function of the WRF model is to simulate the atmospheric transport. This simulation was run for the January–April 2015 time period using unscaled emissions from 2012 that were shifted by a few days to



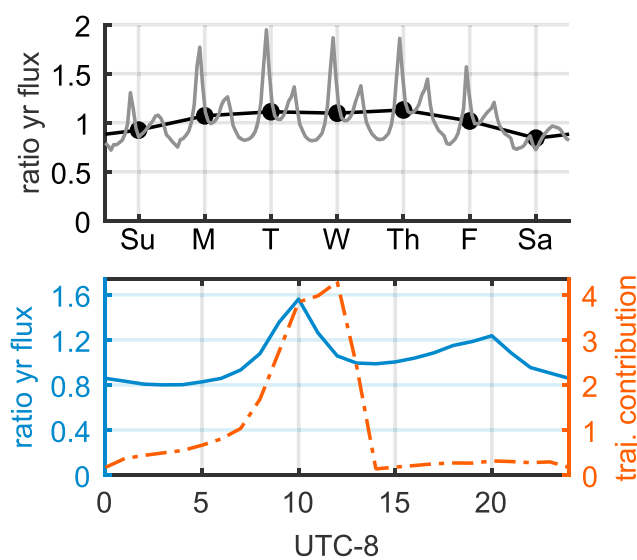


**Figure 2.** Time variation of Hestia-LA v1.0 fossil fuel emissions over the time period of this study (January–April 2015). (top) Average daily or hourly emissions compared to yearly average. Dots are daily averages centered on local noon. Higher emissions are shown for weekdays compared to weekends. (bottom) Average diurnal profile of emissions compared to yearly average. On the right axis is the normalized temporal contribution of air parcels passing through the ML in the SoCAB to measurements at 1300 (UTC-8).

much of a difference in  $X_{\text{CO}_2}$  is there between Caltech and JPL if at any moment in time the  $\text{CO}_2$  mixing ratio is uniform throughout the ML, and the ML height (asl) is the same at both locations? It does not provide a full description of the atmosphere, and a more detailed description is in the supporting information [McKain et al., 2012; Ware et al., 2016; Newman et al., 2013; Verhulst et al., 2016; Hersey et al., 2013]. This model provides a third and final source of simulated  $X_{\text{CO}_2}$ .

In the toy model, we assume  $\text{CO}_2$  is uniform both horizontally and vertically in the ML. The ML height is set to vary diurnally with a Gaussian shape each day. We also include an independent diurnal change in the ML  $\text{CO}_2$  mixing ratio driven primarily from dilution by free tropospheric air and uptake by the biosphere [Newman et al., 2013] that varies with time of year. The range of the model ML  $\text{CO}_2$  enhancement values above that in the free troposphere is in line with those seen at urban LA sites [Verhulst et al., 2016]. Free tropospheric  $\text{CO}_2$  levels are obtained using the TCCON a priori profiles. The model was run over the years 2011–2015.

In the toy model, the difference in  $X_{\text{CO}_2}$  between Caltech and JPL is due solely to differences in the terrain height. The total column abundances over higher-altitude terrain contain a smaller fraction of the ML relative to the entire column, and thus, we expect  $X_{\text{CO}_2}$  to decrease with increasing surface altitude. A basic cartoon of the model relating Caltech and JPL  $X_{\text{CO}_2}$  at different times of the day is shown in Figure 3.

### 3. Temporal Variations and Persistent Enhancements

#### 3.1. Diurnal Variation

Wunch et al. [2009] noted significant diurnal variations in  $X_{\text{CO}_2}$ ,  $X_{\text{CH}_4}$ , and  $X_{\text{CO}}$  measured at the JPL TCCON site. Though we focus on  $X_{\text{CO}_2}$ , we include other gases for reference. The diurnal variations for all these gases are highly correlated due to the advection within the basin. In Figure 4 are example diurnal profiles, which show larger diurnal variations and larger DMFs at Caltech than at other sites. Chen et al. [2016] have also made column DMF observations around Pasadena using EM27/SUN spectrometers and noted similar features in the diurnal profiles. The average diurnal difference between sites is shown in Figure 5. We assume, as did Wunch et al. [2009], that the differences in  $X_{\text{CO}_2}$  between sites are caused by enhancements near the surface, and so the differences have been divided by the surface averaging kernels of the measurements. For Figure 5 these data were filtered as described in Appendix B to show only “typical” differences. These data sets do not necessarily cover the same time periods.

maintain the correct day of week. This WRF model has an extent of  $228 \times 228$  grid boxes over and around the SoCAB. For the March–April time period, we also explored simulations that have uniform emissions across the full WRF domain [see Feng et al. [2016], Figure 1a]. This model provided two simulated  $X_{\text{CO}_2}$  fields, (1) from Hestia FF emissions and (2) from uniform emissions.

To compare the WRF results with measured data, we use the WRF grid box with a center point nearest the measurement site. The center coordinates for the Caltech box are  $34.134^\circ\text{N}$ ,  $118.123^\circ\text{W}$ , 212 m asl. The center coordinates for the JPL box are  $34.199^\circ\text{N}$ ,  $118.172^\circ\text{W}$ , 376 m asl. The center coordinates for the AFRC box are  $34.960^\circ\text{N}$ ,  $117.879^\circ\text{W}$ , 688 m asl.

#### 2.5. Simple $\text{CO}_2$ Model

In addition to the full physics WRF simulations, we consider a simple “toy” model to estimate  $X_{\text{CO}_2}$  gradients due to topography. It was constructed for only one purpose, namely, to answer how

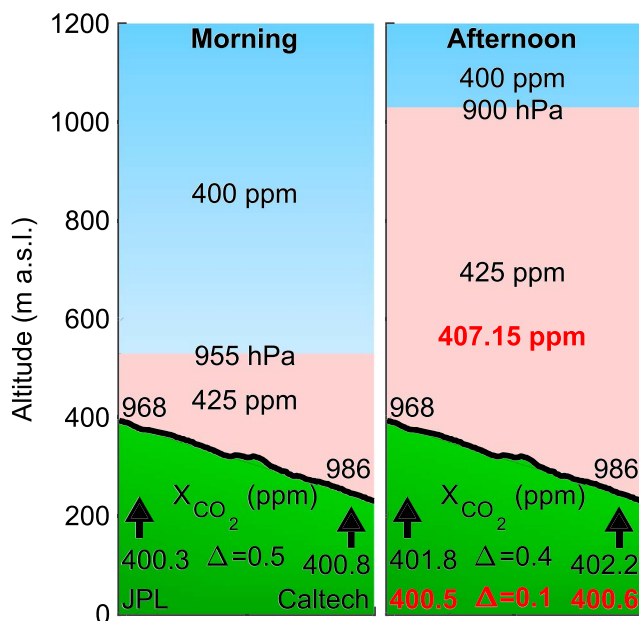


**Figure 3.** A cartoon visualization of the simple toy model which has two above ground layers (the ML and everything above the ML). The average ML height is flat with pressure in the model. The text labels show various pressures and average CO<sub>2</sub> mixing ratios. At the bottom are column abundances and their differences at the Caltech and JPL sites. Values in red for the afternoon are for the case when excess CO<sub>2</sub> is mixed into a deeper layer.

There are several possible mechanisms that drive these diurnal patterns. JPL is an area with more vegetation than Caltech, and so some of the higher  $X_{CO_2}$  difference in the mornings compared to afternoons is likely due to respiration from the biosphere at night [Djuricin et al., 2010; Newman et al., 2013]. The difference in  $X_{CO_2}$  compared with the AFRC site can be attributed to a growth of the ML until midday, after which the ML height decreases and the difference returns to morning levels. The  $X_{CH_4}$  difference in Figure 5 between Caltech and JPL is similar to the Caltech-AFRC difference in the morning. This feature could be from air with high methane loading being advected from the California San Joaquin Valley, where there is high agricultural activity, to the AFRC site. Typically,  $X_{CO_2}$ ,  $X_{CH_4}$ , and  $X_{CO}$  are enhanced at Caltech relative to AFRC and JPL. Enhancements compared to AFRC can be attributed to polluted air being trapped in the basin. An increase in the ML height above Caltech may cause the difference compared to AFRC to (1) increase if polluted air

flows horizontally to fill the rising ML, (2) decrease if the ML increases enough for polluted air to flow out of the basin over the mountains, or (3) stay the same if the polluted air is simply mixed vertically into a deeper ML.

Interestingly, differences between Caltech and JPL are, at certain times of the day, about as large as the differences between Caltech and AFRC, despite the JPL site also being within the basin and its proximity to Caltech.

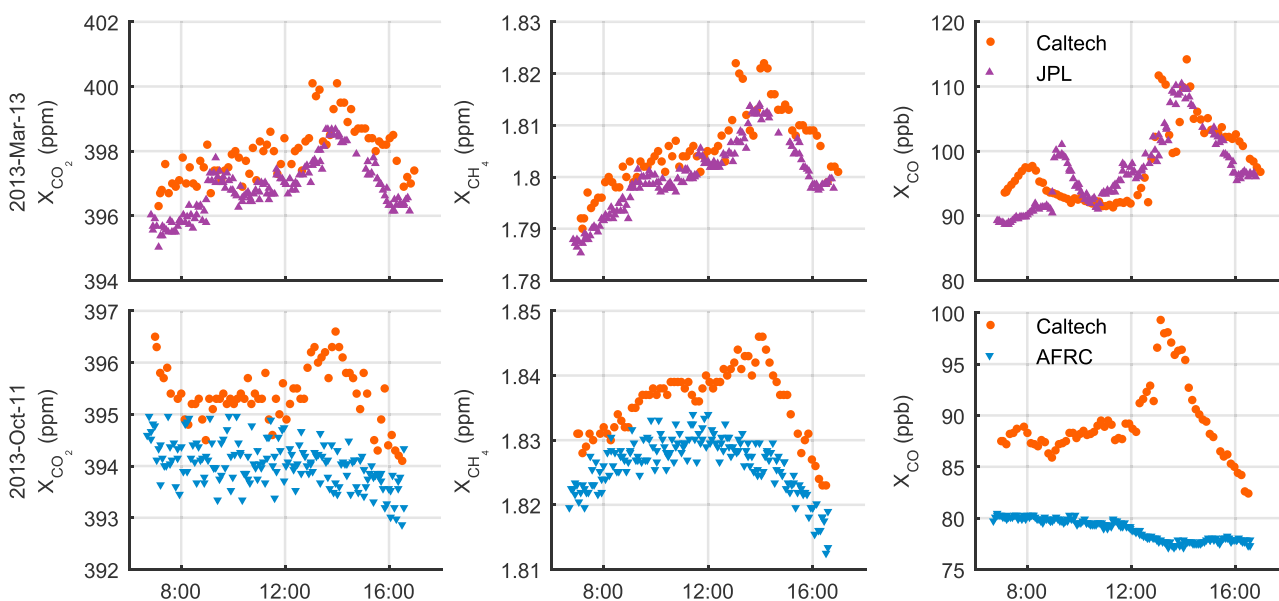


**Figure 4.** Example diurnal profiles of TCCON observations. Variations in column DMFs of different gases at the Caltech site are correlated. DMFs tend to be largest at Caltech. Caltech and JPL variations are similar. AFRC variations throughout the day are smaller and primarily from synoptic scale variability. In Figure 5 are differences between sites.

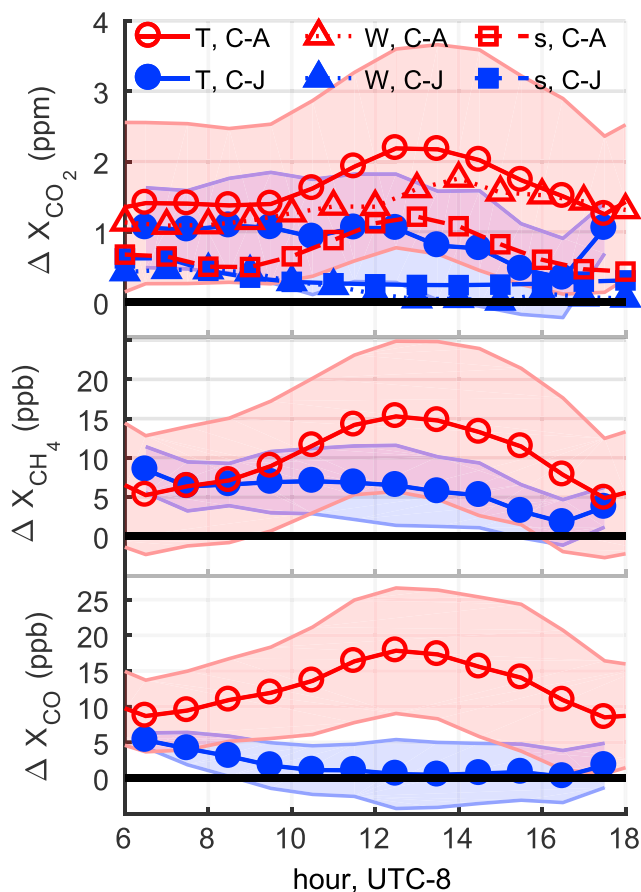


**Figure 5.** Diurnal differences in  $X_{gas}$  between sites from measured and modeled data over their respective time series. TCCON observations were filtered as described in Appendix B to give typical diurnal profiles. T = TCCON, W = WRF+Hestia-LA, s = simple model (Figure 3), C-J = Caltech-JPL difference, C-A = Caltech-AFRC difference. Error bars ( $1\sigma$ ) are shown for the TCCON differences but are omitted from model values for clarity. (top)  $X_{CO_2}$  differences. TCCON  $\sigma_{C-J} = 0.7$  ppm,  $\sigma_{C-A} = 1.3$  ppm. WRF  $\sigma_{C-J} = 0.5$  ppm,  $\sigma_{C-A} = 1.0$  ppm. Simple model  $\sigma_{C-J} = 0.1$  ppm,  $\sigma_{C-A} = 0.2$  ppm. (middle)  $X_{CH_4}$  differences. TCCON  $\sigma_{C-J} = 3.8$  ppb,  $\sigma_{C-A} = 8.7$  ppb. (bottom)  $X_{CO}$  differences. TCCON  $\sigma_{C-J} = 3.4$  ppb,  $\sigma_{C-A} = 7.8$  ppb.

sets by their surface averaging kernels from measurements within the basin. For OCO-2 nontarget mode SoCAB data, any point within 60 km is used for comparison. For times when OCO-2 targeted the Caltech site and obtained many nearby observations, we only use data within 5 km of Caltech. This approach yields a similar number of observations for target and nontarget overpasses; if only target observations were used, the basin average enhancement is larger.

The Caltech-AFRC and Caltech-JPL differences with time in the TCCON  $X_{CO_2}$  are shown in Figure 7. In general,  $X_{CO_2}$  measured at Caltech is greater than at JPL or AFRC. In late spring of 2014, and winters of 2015 and 2016, there are lower enhancements of  $X_{CO_2}$  than at other times of year observed in the TCCON data. As noted in previous studies, the air trajectories to Caltech vary with season [Newman et al., 2016; Verhulst et al., 2016] and this likely contributes to the variability with more efficient ventilation of the basin during times of lower enhancements. The  $X_{gas}$  variability is weaker in the  $X_{CO}$  and  $X_{CH_4}$  data. The WRF data match in 2015, but the model time period is too short to observe the annual variability. The changes in  $X_{CH_4}$ ,  $X_{CO}$ ,  $X_{H_2O}$ , and wind trajectories indicate that part of the  $X_{CO_2}$  fluctuations is due to atmospheric transport. Some of the  $X_{CO_2}$  variability is likely due to the biosphere of the SoCAB. Because of landscaping, there is significantly more vegetation within the SoCAB than at AFRC, and artificial irrigation may affect  $CO_2$  seasonality [Newman et al., 2016].

Over their full time series, the enhancement compared to JPL is about one third of that compared to AFRC. The enhancement relative to AFRC can be ascribed to the proximity of sources and to polluted air being trapped within the basin. However, this enhancement compared to AFRC can vary depending on the origins of the air masses which changes throughout the year [Verhulst et al., 2016]. This can also affect the intra-basin enhancements—ML air masses less enhanced in  $CO_2$  will lead to smaller horizontal gradients in  $X_{CO_2}$ . We examine the Caltech-AFRC difference in the next section. We explore reasons for the differences between Caltech and JPL in section 4.

**3.2. Full Time Series**

Here we focus on quantifying the  $X_{CO_2}$  enhancement in the SoCAB relative to background. We use observations at approximately 1300 (UTC-8) when the ML height is generally stable and well developed, and the error due to the ML height determination in the WRF model is at a minimum [Feng et al., 2016]. This is also the approximate time OCO-2 makes observations within the SoCAB on some days. An example of OCO-2 target data of the Caltech and AFRC sites is shown in Figure 6.

Data from different sites and data sets were first averaged into 1 week time bins, before calculating differences. Because we assume most of the difference between locations inside and outside the basin are near the surface, we divide the TCCON and OCO-2 data

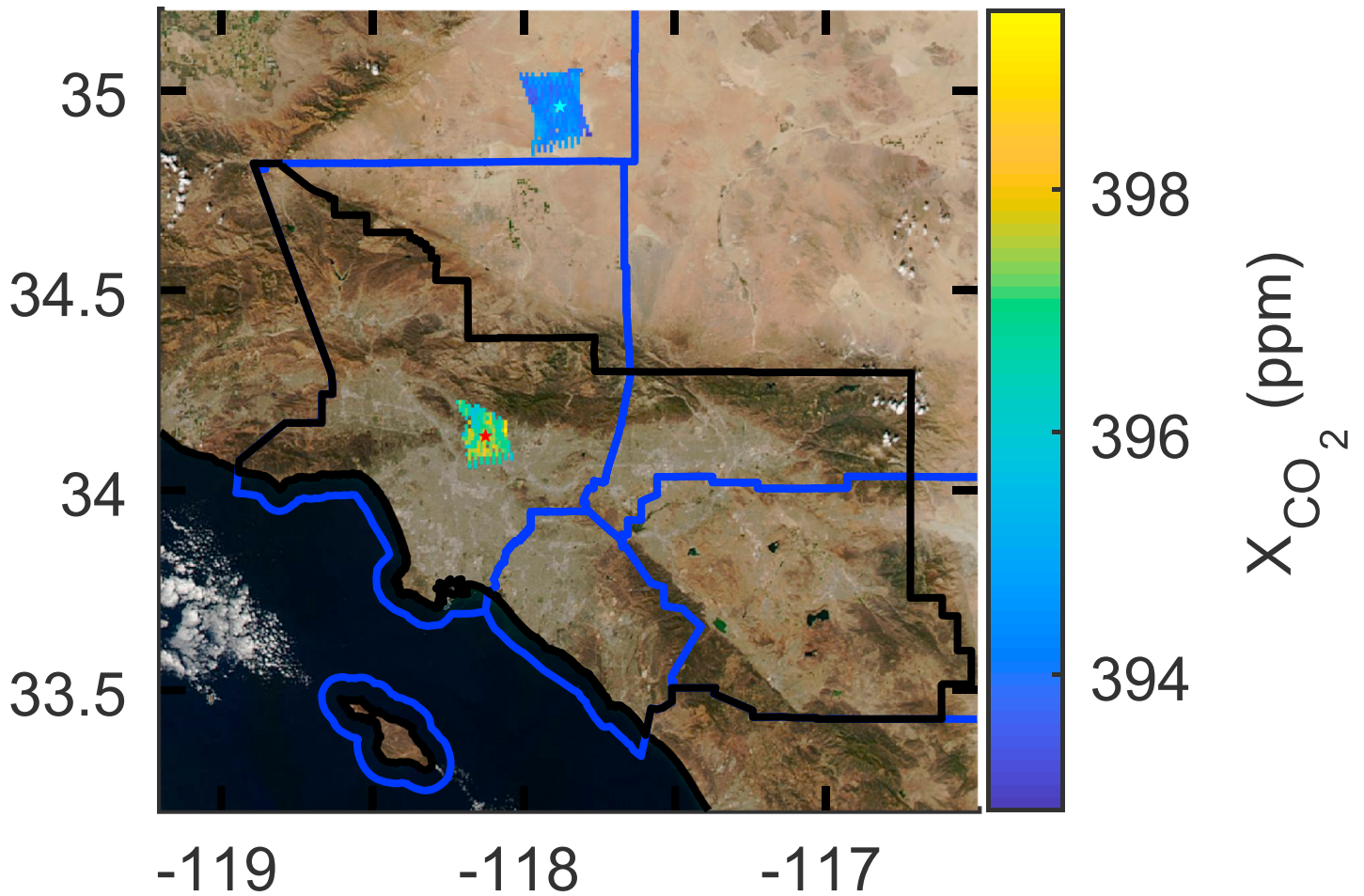


**Figure 6.** An example of target mode data from 19 September (Caltech) and 21 September (AFRC) 2014 overlaid on the Moderate Resolution Imaging Spectroradiometer image from 21 September 2014. These data were averaged into  $0.01 \times 0.01^\circ$  bins.

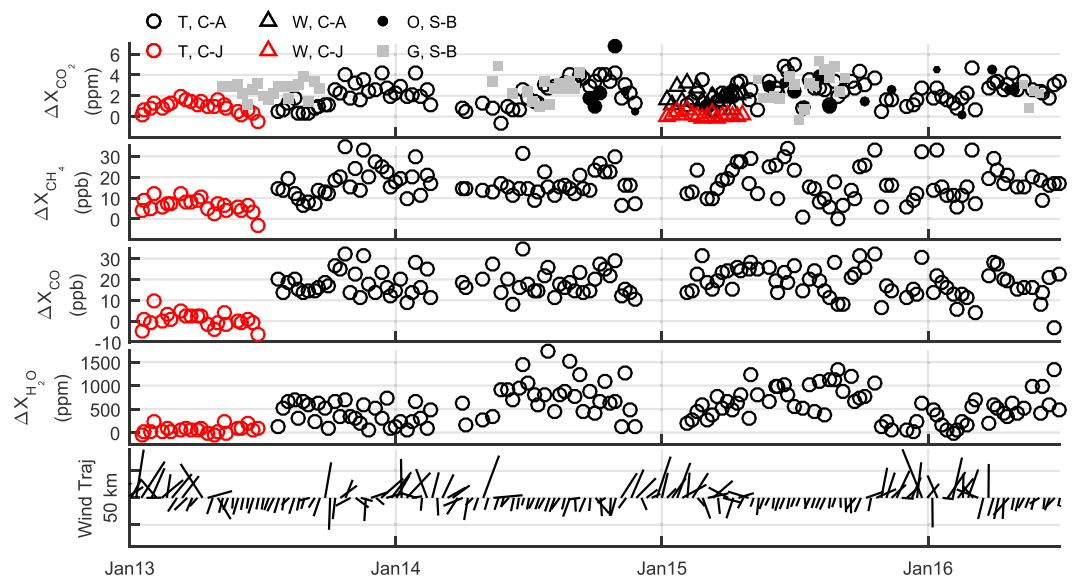


**Figure 7.** Time series of differences between data at different locations. T = TCCON, W = WRF, O = OCO-2, G = GOSAT, C = Caltech, A = AFRC, J = JPL, S = SoCAB, and B = background. OCO-2 and GOSAT points are sized according to distance from Caltech, with points further away represented by smaller dots. Wind vectors in the bottom panel point to the direction the wind at 500 m asl originated from at 50 km from Caltech.



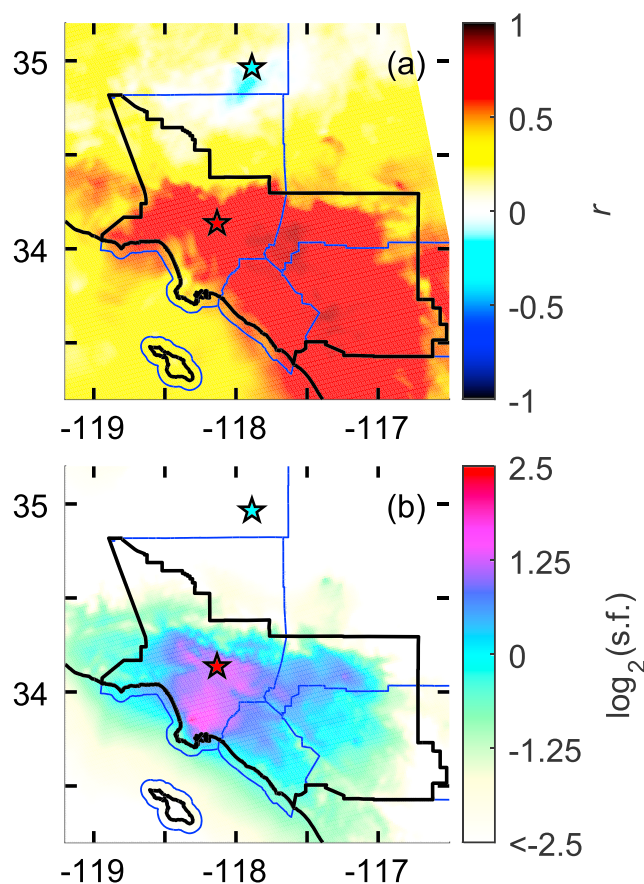


**Figure 8.** Comparisons between individual pixels and basin averaged fossil fuel  $X_{CO_2}$  from the simulated WRF data at 1300 (UTC-8). Shown are averages across all days. (a) Correlation coefficients between pixels and the basin average tend to be closer to 1 toward the east central part of the basin. (b) Scaling factors of basin compared to individual points. Points near the Palos Verde Peninsula are 3.5 times as large as the SoCAB on average. Points near Caltech are 2.3 times as large as the SoCAB average.

118.2°W) where GOSAT frequently made observations during 2009–2010. Toward the central and eastern ends of the basin, the magnitude of the ratio  $X_{CO_2,local}:X_{CO_2,SoCAB}$  depends on the terrain, with larger ratios (or scaling factors) where the surface altitude is lower. To track small changes in  $X_{CO_2}$  enhancements that are related to changes in emissions requires the enhancements to be larger than the measurement sounding uncertainty and to correlate with the region emissions as a whole.

**3.3. Persistent Enhancements**

GOSAT-ACOS v2.9 level 2  $X_{CO_2}$  data within the basin have a robust  $3.2 \pm 1.5$  ( $1\sigma$ ) ppm ( $n = 34$ ), enhancement compared to the  $X_{CO_2}$  observed over the desert from June 2009 to August 2010 [Kort et al., 2012]. Results were similar for other studies using GOSAT observations ( $2.75 \pm 2.86$  ( $1\sigma$ ) ppm,  $n = 8$ ) [Janardanan et al., 2016]. Kort et al. [2012] estimated that a 0.7 ppm change in  $X_{CO_2}$  (22% of emissions) could be detected using GOSAT observations on a yearly timescale. We repeat the analysis using the GOSAT-ACOS v7.3 data, and average weekly rather than in 10 day blocks. Over the same time we find a similar enhancement of  $2.9 \pm 2.0$  ( $1\sigma$ ) ppm. When we also include similar latitudinal ocean observations as background with a 21 day adjustment to better match the AFRC TCCON data, the enhancement is  $2.3 \pm 1.8$  ( $1\sigma$ ) ppm. Over the full June 2009–May 2016 time period the SoCAB enhancement determined by GOSAT observations is  $2.4 \pm 1.6$  ( $1\sigma$ ) ppm ( $n = 118$ ). Enhancements observed by the OCO-2 satellite are similar at  $2.4 \pm 1.5$  ( $1\sigma$ ) ppm ( $n = 26$ ).

Average differences from weekly averaged TCCON data are shown in Table 1. We emphasize that the Caltech-JPL  $X_{CO_2}$  difference is a significant fraction (~40%) of the Caltech-AFRC difference. Site-to-site biases

Newman et al. [2013] calculated that at the surface, 50% of excess  $CO_2$  in Pasadena at night is from soil and plant respiration, which is presumably balanced throughout the year by uptake during the daytime. Because there are coincident observations for Caltech and JPL for only ~6 months, this limits our understanding of the intra-SoCAB difference. The Caltech-JPL difference has a profile that peaks in spring, with lower enhancements in the early and midyear. This behavior could arise from air masses originating from the desert in winter, and higher ML heights in summer which could decrease the ML to free troposphere gradients and hence the spatial  $X_{CO_2}$  differences.

If observations are concentrated at one location, they may not match basin-wide variations both in magnitude and in variation. Thus, in Figure 8 we plot correction coefficients for variations in  $X_{CO_2}$  between single grid points and the average  $X_{CO_2}$  for the SoCAB as a whole using the WRF simulations. These variations are for 1300 (UTC-8), and  $X_{CO_2}$  at the AFRC site has been subtracted as background. Locations toward the center of the basin and toward the southeast are most correlated with the basin as a whole. However, the largest  $X_{CO_2}$  enhancements are observed more toward the west; the western part of the basin is also where the majority of oil and gas exploration occurs. Typical  $X_{CO_2}$  values are 3 times as large as the basin average just north of the Palos Verdes Peninsula (~33.9°N,

**Table 1.** TCCON  $X_{\text{gas}}$  Differences

	Difference	$1\sigma$
<i>Caltech-AFRC<sup>a</sup></i>		
$X_{\text{CO}_2}$ (ppm)	2.3	1.2
$X_{\text{CH}_4}$ (ppb)	17	8
$X_{\text{CO}}$ (ppb)	19	7
<i>Caltech-JPL<sup>b</sup></i>		
$X_{\text{CO}_2}$ (ppm)	0.9	0.6
$X_{\text{CH}_4}$ (ppb)	6	3
$X_{\text{CO}}$ (ppb)	0.6	3.5

Differences in  $X_{\text{gas}}$  observed using weekly averaged TCCON data at 1300 (UTC-8)  $\pm 1$  h.

<sup>a</sup>From August 2013 to June 2016 ( $n = 128$ ).

<sup>b</sup>From January 2013 to June 2013 ( $n = 22$ ).

on order of 0.1–0.2 ppm may exist among TCCON sites which could bias these enhancements [Hedelius *et al.*, 2017]. The CARB reported CO emissions of 0.91 Gg CO yr<sup>-1</sup> for 2012 (<https://www.arb.ca.gov/app/emsmv/2013/emssumcat.php>), and 160 Gg CO<sub>2</sub> yr<sup>-1</sup> after scaling state emissions by 0.42 for the population only in the SoCAB (<https://www.arb.ca.gov/cc/inventory/data/data.htm>). The inventory estimated that CO:CO<sub>2</sub> emission ratio is 9.0 (ppb ppm<sup>-1</sup>). Observed ratios are 8.3 and 0.7 (ppb ppm<sup>-1</sup>) for the Caltech-AFRC and Caltech-JPL differences, respectively. The Caltech-AFRC is in agreement with the inventory ratio, and the ratio of 11 (ppb ppm<sup>-1</sup>) from Wunch *et al.* [2009]. The CO enhancements for Caltech-JPL are lower than expected for reasons not fully understood.

## 4. Spatial SoCAB Variations

In this section we seek to answer what causes  $X_{\text{CO}_2}$  variability on the scale of a few kilometers in the SoCAB as noted from section 3? This increased variation can also be seen in OCO-2 data, with a median standard deviation of 1.04 (90% confidence interval (CI): 0.60, 1.71) ppm for points within 9 km, compared with 0.68 (90% CI: 0.48, 1.70) ppm for the desert. We focus on emissions, dynamics, and topography to explain this variability. For example, the enhancement at Caltech relative to the nearby JPL site may be due to a combination of emission source locations and dynamics, we consider these effects separately in section 4.1 and 4.2. Caltech is closer to downtown Los Angeles, and polluted plumes of air may not reach JPL before being advected eastward. In section 4.3 we consider the impact of topography on  $X_{\text{gas}}$  in areas where the in situ DMF in the ML differs significantly from the rest of the column. A discussion of average surface CO<sub>2</sub> and the relationship with general wind patterns and topography is available from Feng *et al.* [2016] (section 4 therein).

### 4.1. Local Emissions and $X_{\text{CO}_2}$ Variance

The relationship between nearby Hestia FF emissions and simulated  $X_{\text{CO}_2}$  from the WRF data set is analyzed. For each grid box in the WRF model output we calculate Pearson's  $r$  correlation coefficient between the simulated  $X_{\text{CO}_2}$  product generated by advecting Hestia emissions and the raw Hestia v1.0 emissions themselves for the set of spatially close points. The radii defining the small area of spatially close points are varied from 1.3 km to 30 km. We compute the average value of  $r$  at 1300 (UTC-8). We use  $r$  as an indicator of correlation because (1) it is unaffected by scaling factors—for example, it would not change if all emissions were doubled—and (2) it is unaffected by a constant offset, eliminating the need for a background value. If point source emissions were constant at all times and there were no wind and diffusion (i.e., no transfer of CO<sub>2</sub> between boxes), it would be expected that the surface flux into each box would explain all variance among boxes and  $r(X_{\text{CO}_2}, \text{FF}) = 1$ . In the data, we note only a weak  $r$ . The largest values ( $\sim 0.18$ ) are for areas with a radius <4 km and minimum FF emission gradients of at least 1 g CO<sub>2</sub> m<sup>-2</sup> h<sup>-1</sup>. This suggests that the size of emission sources in each box by itself is only a weak predictor of  $X_{\text{CO}_2}$  variance.

### 4.2. Dynamical Influences on $X_{\text{CO}_2}$ Variability

To estimate the impact of dynamics on the variation of  $X_{\text{CO}_2}$  within the basin, we analyze simulations performed with geographically uniform fluxes over the full WRF domain driven by the same dynamics as the simulations using Hestia-LA v1.0. We compare with the advected Hestia-LA v1.0 product, which is taken as “truth” and denoted  $X_{\text{CO}_2}$ . If polluted air accumulates in the ML in the same locations due to meteorology without regards to the locations of emission sources, we would expect  $r(X_{\text{CO}_2}, X_{\text{CO}_2, \text{uniform}}) = 1$ .

We observe no significant correlation between these products on scales of 1.3 km to 30 km across the basin ( $r$  values,  $Md$ : -0.045, 90% CI: -0.250, 0.161). There was also no significant correlation for the points north

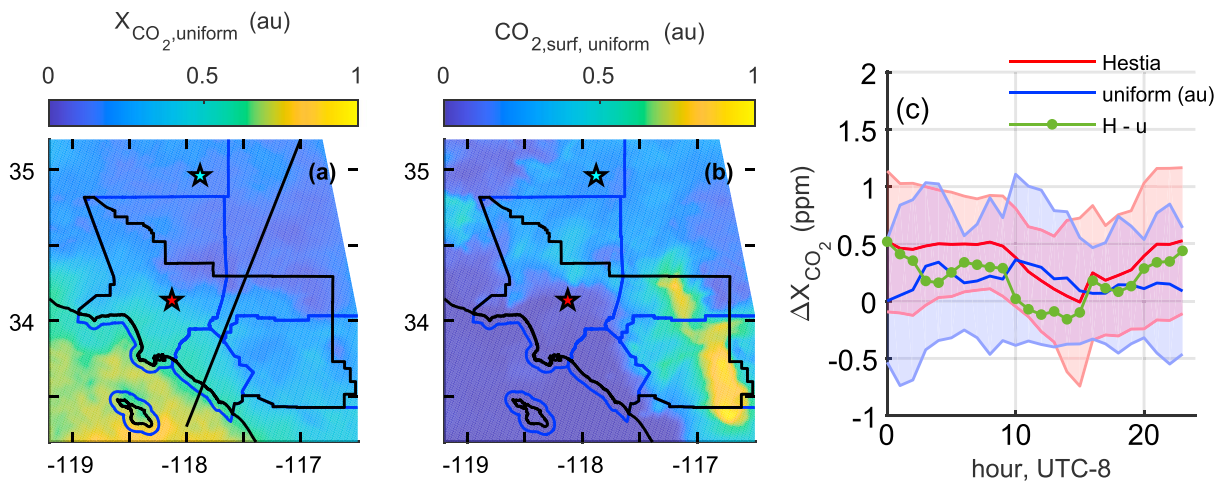


**Figure 9.** Maps of 1300 (UTC-8) average uniform emission products. au = arbitrary units (a) simulated  $X_{CO_2}$  for the uniform emission product. The higher ocean values are due to contributions above the ML, and a wind vector is shown in SI Figure S5 for the black line shown. (b) simulated  $CO_2$  at the surface. (c) Differences in simulated  $X_{CO_2}$  between the Caltech and JPL sites. The diurnal profiles differ between simulations using Hestia versus uniform emissions. Error bars are  $1\sigma$ .

of and within 9 km of Caltech ( $Md$ :  $-0.009$ , 90% CI:  $-0.766, 0.712$ ). In Figure 9 are maps of the average  $X_{CO_2}$  and surface  $CO_2$  for the uniform emissions case. (For the uniform emissions case we use arbitrary units which should not matter so long as there is no numerical diffusion in the model.) Over the ocean,  $X_{CO_2}$  is enhanced due to high  $CO_2$  above the ML from return winds aloft (see supporting information Figure S5). Because emissions were uniform over the entire domain, this air with enhanced  $CO_2$  from the desert region also contributes to the larger  $X_{CO_2}$  values seen over the ocean. If the surface  $CO_2$  is taken as a first-order approximation of how  $X_{CO_2}$  would behave without emissions from the desert, we see that enhanced  $CO_2$  is seen in the eastern parts of the SoCAB. However, the finer features that relate with topography in Figure 10 are not seen in Figure 9.

Dynamics alone do not explain a significant fraction of the difference observed between the Caltech and JPL sites. An extension of this test we did not try would be to include uniform emissions only within the geographical SoCAB boundaries and see how they relate when compared with the Hestia run. The distribution of emission sources needs to be considered concurrently with dynamics to explain  $X_{CO_2}$  variations in the SoCAB.

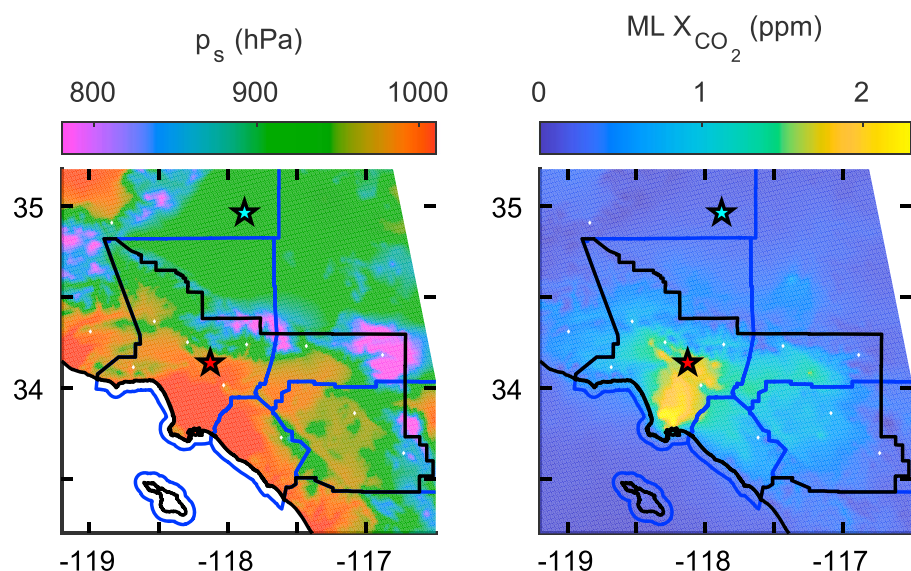


**Figure 10.** Averages from the WRF simulation at 1300 (UTC-8). (a) Average surface pressure and (b) the contribution of ML  $CO_2$  to the total column. Over areas  $\sim 0.1^\circ$  many features in the surface pressure map are reflected in the ML  $X_{CO_2}$ . This could arise from different fractional contributions of the ML to the total column (see Figure 3). Small white diamonds shown are to highlight some areas where this can be seen more clearly.

### 4.3. Terrain Effects

To the extent that the same excess  $\text{CO}_2$  is simply mixed into a deeper ML, column measurements are insensitive to ML height [Yang *et al.*, 2007]. For areas with ML DMFs that are enhanced compared to free tropospheric levels, this causes in situ DMFs within the ML to drop and become closer to free tropospheric levels as the ML height increases [McKain *et al.*, 2012; Newman *et al.*, 2013]. However, if the fractional change in ML height is different between sites, the column difference will also change. This is considered in the “toy” model (Figure 3). Note that Figure 3 also provides a numerical example of this concept. Going from morning to afternoon requires a horizontal flow of  $\text{CO}_2$  from Caltech to JPL. If the surface were at a uniform altitude, the  $\Delta$  between Caltech and JPL would be zero.

Differences in the ML height above ground level explain part of the variation in  $X_{\text{CO}_2}$  between Caltech and JPL. Part of the remaining discrepancy is because  $\langle \text{CO}_2 \rangle_{\text{ML}}$  (where bracket notation indicates the average here) is not the same at both locations. This model further assumes that the ML height is at the same pressure height  $p_{\text{ML}}$  at both locations. This assumption is better inland than closer to the coast—for example, Ware *et al.* [2016] noted a sharp transition in ML height between the shallow marine layer (about 2–3 km onto land) and the convective regime further inland. Though the ML may fluctuate by a few hundred meters over a distance of several kilometers due to updrafts [Nielsen-Gammon *et al.*, 2008], these are averaged out with downdrafts over an hour or so. Over smaller areas, average variations in the ML height pressure are smoother than changes in surface pressure as noted by streamlines over topographic features [Perry and Snyder, 2017]. Maps of the average surface pressure  $p_s$  and ML  $X_{\text{CO}_2}$  are shown in Figure 10. Over small areas  $\sim 0.1^\circ$  many features are reflected in the average ML  $X_{\text{CO}_2}$  at 1300 (UTC-8).

$X_{\text{CO}_2}$  ( $c$ ) can be calculated by considering the weighting of the ML and the rest of the column separately:

$$c = \frac{p_s - p_{\text{ML}}}{p_s} \langle \text{CO}_2 \rangle_{\text{ML}} + \frac{p_{\text{ML}}}{p_s} \langle \text{CO}_2 \rangle_{\text{aboveML}} \quad (2)$$

where  $\langle \text{CO}_2 \rangle_{\text{aboveML}}$  is the average  $\text{CO}_2$  DMF from the top of the ML to the top of the atmosphere. Equation (2) can be rewritten as

$$c = \langle \text{CO}_2 \rangle_{\text{ML}} + \frac{p_{\text{ML}}}{p_s} (\langle \text{CO}_2 \rangle_{\text{aboveML}} - \langle \text{CO}_2 \rangle_{\text{ML}}). \quad (3)$$

If the above assumptions were perfect, then all variation in  $X_{\text{gas}}$  between locations would be linearly related with  $p_s^{-1}$ . If  $\langle \text{CO}_2 \rangle_{\text{ML}} > \langle \text{CO}_2 \rangle_{\text{aboveML}}$ , then the correlation is negative.

We evaluate this relationship using  $r$  over small areas with the simulated FF  $X_{\text{CO}_2}$  from the WRF model. We choose 1300 (UTC-8) as the analysis time because it is local midday when the ML is more stable, and it corresponds to the approximate time of OCO-2 and GOSAT measurements. Figure 11 includes a map of  $r(X_{\text{CO}_2}, p_s^{-1})$  for areas of radii 9 km for 9 March 2015 and  $\nabla p > 7$  hPa. In general, we note a strong negative relationship in areas within the SoCAB where the terrain changes rapidly. For example,  $r < -0.5$  toward south side of the San Gabriel Mountains ( $\sim 34.2^\circ\text{N}$ ) and around the Santa Ana Mountains at  $33.7^\circ\text{N}$  and  $117.5^\circ\text{W}$ . The relationship is weaker toward the peak of the San Gabriel range. Toward the base of the San Gabriel range on the northern side, we note a positive relationship in places. The increase in  $X_{\text{CO}_2}$  with the surface altitude may be from basin outflow, where further distances from the basin coincide with a decrease in altitude. We also note strong negative relationships toward the southern end of the California Central Valley ( $35^\circ\text{N}$  and  $119^\circ\text{W}$ ). The correlation coefficient  $r$  is highly variable across the Mojave desert surrounding the AFRC site.

We analyze the mean  $r$  in the SoCAB for different small area radii and different minimum pressure differences for four different months (Figure 11). On average  $r$  is negative, with stronger correlations for smaller areas as well as over areas with larger pressure differences. Across the full basin for 9 km areas the median is  $-0.37$  (90% CI:  $-0.52, -0.15$ ). The correlation becomes weaker in April as the temperature increases and the ML becomes less stable. For points north of (where terrain is steeper), and within 9 km of Caltech, the median for January to April is  $r = -0.45$  ( $\pm 1\sigma$  CI:  $-0.76, -0.04$ ). The median coefficient of determination ( $R^2$ ) is thus 20% ( $\pm 1\sigma$  CI: 0%, 58%), suggesting about 20% of the variance in  $X_{\text{CO}_2}$  between Caltech and JPL can be explained by changes in topography.

The toy model (Figure 3) provides another measure for how much of the  $X_{\text{CO}_2}$  difference can be explained by differences in surface altitude. Based on the current parameterization of the simple model, the median ratio



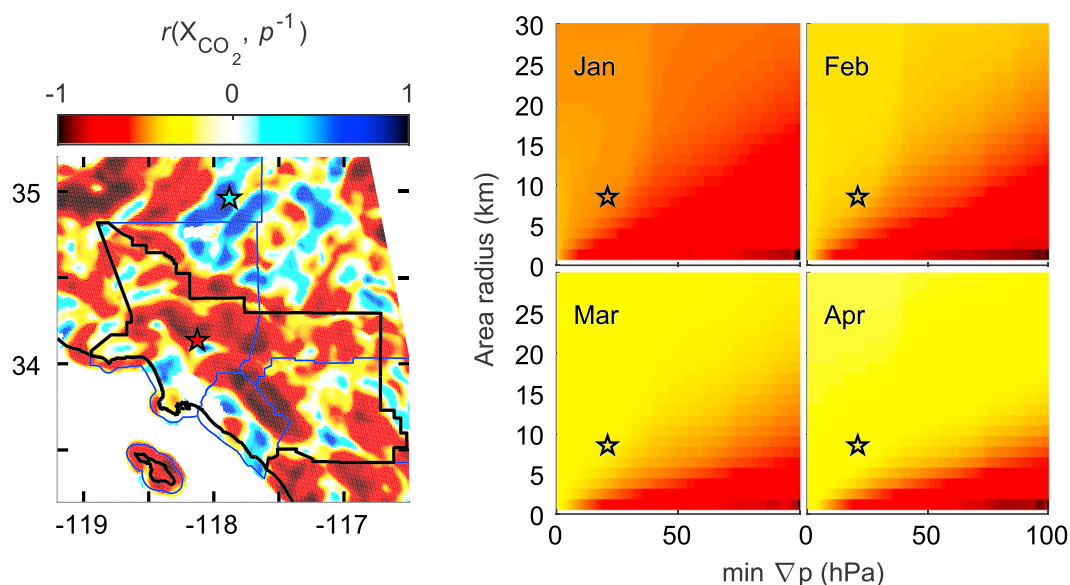


**Figure 11.** Correlation coefficients relating  $X_{CO_2}$  and  $p^{-1}$ . Large negative correlations (red) indicate that increases in  $X_{CO_2}$  are highly correlated with lower surface heights. (left) Shown spatially for areas of radii 9.1 km (approximately seven WRF boxes). Data are from 9 March 2015, 1300 (UTC-8). Correlations are stronger over steeper terrain. (right) Correlation as functions of area radii and minimum pressure differences (rather than spatially). Shown are averages over the entire SoCAB for data from 1300 (UTC-8). The star marks the distance and  $\nabla p$  between Caltech and JPL. Starting in the bottom right corners (large  $p$  gradient, small radius) the correlation is strong. Going up (larger radii) the correlation weakens. Going right to left (smaller minimum  $p$  gradient) the correlation also weakens.

between model:measured values is 36% ( $\pm 1\sigma$  CI: 10%, 101%). A site-to-site TCCON bias of up to  $\pm 0.2$  ppm would make the median value 29–46% [Hedelius et al., 2017]. Thus, approximately 36% of the  $X_{CO_2}$  difference between Caltech and JPL can be attributed to differences in altitude alone using this simulation.

### 5. Conclusions

Observations of  $X_{CO_2}$  within the SoCAB are enhanced compared to the nearby Mojave Desert. This typical enhancement is due to the proximity of anthropogenic sources of  $CO_2$  combined with the basin topography which can lead to the trapping of polluted air. Enhancements of  $X_{CO_2}$  within the SoCAB are  $2.3 \pm 1.2$  ( $1\sigma$ ) ppm based on the TCCON observations. OCO-2 v7r enhancements are similar ( $2.4 \pm 1.5$  ( $1\sigma$ ) ppm). These are smaller than the  $3.2 \pm 1.5$  ( $1\sigma$ ) ppm derived from GOSAT observations by Kort et al. [2012] but is more in line with the  $2.75 \pm 2.86$  ( $1\sigma$ ) ppm results of Janardanan et al. [2016]. We also observed lower enhancements with GOSAT-ACOS v7.3 data ( $2.4 \pm 1.6$  ( $1\sigma$ ) ppm) over a longer time period with a different seasonal sampling weighting. There is also seasonality in the TCCON data, but it is not apparent in the GOSAT observations, which may be because air in Pasadena is more strongly influenced by seasonal wind patterns. All of the basin enhancements from different observation sets are within  $1\sigma$  agreement.

There is significant  $X_{CO_2}$  variation within the SoCAB, even in locations less than 10 km apart. Between the Caltech and JPL TCCON sites, the difference is  $0.9 \pm 0.6$  ( $1\sigma$ ) ppm, which is a significant fraction ( $\sim 40\%$ ) of the Caltech-AFRC difference. Both dynamics and the locations of sources need to be considered simultaneously to account for these variations. Topography also appears to play a significant role in some locations in the basin. Using the difference in  $X_{CO_2}$  between Caltech and JPL, we estimate 20% ( $\pm 1\sigma$  CI: 0%, 58%) (from the WRF analysis, section 4.3) to 36% ( $\pm 1\sigma$  CI: 10%, 101%) (from our simple climatology model) of the difference is explained by changes in topography alone. Though other factors such as emissions and dynamics together explain more than half of the difference, topography changes in the presence of a sharp gradient between the mixed layer and free troposphere contribute significantly to the difference.

The importance of topography in driving variation in  $X_{CO_2}$  has implications beyond the urban area studied here. Such influence is undoubtedly important in forested and agricultural regions as well. Though previous papers have included comments on column measurements having reduced sensitivity to the ML height,

this sensitivity is not zero. Thus, correctly parameterizing the ML is important in models using column measurements. This is especially important for studies of fluxes within small areas using column measurements [e.g., *Chen et al.*, 2016], as errors in the ML height can lead to significant errors in the retrieved fluxes.

## Appendix A: OCO-2 Data, Filtering, and Background

Included in the OCO-2 data set are two types of data quality filters—warn levels (WLs) and a binary  $X_{\text{CO}_2}$  quality flag. WLs are derived using the Data Ordering Genetic Optimization (DOGO) algorithm [*Mandrake and Doran*, 2015a]. Generally, WLs increase as the data quality becomes less reliable. WLs are based on specific retrieval parameters such as surface roughness and the retrieved aerosol optical depth [*Mandrake and Doran*, 2015b]. DOGO also assigns lone outliers to higher WLs [*Mandrake and Doran*, 2015a]. For our analysis we are primarily concerned with lone outliers on scales less than  $\sim 10$  km, which are not always flagged by higher WLs or the binary flag. When included in an inversion, these types of outliers can significantly change flux estimates.

We create a custom filter based on small area analysis. Though this paper focuses on determining reasons for  $X_{\text{CO}_2}$  variations over areas of similar size, the values that are removed by this filter are significantly different from other values in the small area, even though some true variance is expected. Our custom filter is based on analyzing areas of radius  $< 8$  km. We check for low and high outliers. Data are flagged if (1) the furthest points are  $\geq 0.7$  ppm to the next nearest point or (2) the furthest points are  $\geq 0.4$  ppm away with a  $z$  score  $\geq 2.58$  (corresponding to a 99% range). This filter removes an additional 1.3% of data at  $\text{WL} = 0$  and 3.8% of data at  $\text{WL} \leq 14$ . Low outliers are 10–100% more frequent than high outliers. The ratio of high to low outliers is closer to one at lower WLs.

For our analysis we also require background measurements of  $X_{\text{CO}_2}$ . *Kort et al.* [2012] used satellite observations made over the nearby rural desert when calculating the SoCAB  $X_{\text{CO}_2}$  enhancement using observations collected by the GOSAT. This choice was made because the desert is geographically close to the basin which minimizes sensitivity to global or zonal observational bias. We use the TCCON observations at AFRC as background. We also considered ocean observations at similar latitude out to  $179^\circ\text{W}$ , but these OCO-2 observations were shifted in time and biased low in comparison with the AFRC TCCON data. While this bias may reflect real  $X_{\text{CO}_2}$  gradients due to atmospheric dynamics, it may also result from bias between the OCO-2 data taken over land (in nadir and glint modes) versus data taken over the ocean in glint mode only. The comparability of the different modes is being evaluated [*Wunch et al.*, 2017].

## Appendix B: TCCON Data Filtering

For Figure 5 we filtered the binned TCCON data based on what were considered atypical events following methodology similar to *Wunch et al.* [2009]. Days at Caltech with changes in  $X_{\text{CO}_2} > 6.5$  ppm,  $X_{\text{CH}_4} > 40$  ppb or  $X_{\text{CO}} > 30$  ppb were flagged as bad which eliminated 53 of the original 1101 days with measurements from 1 January 2013 onward. Atypical  $\text{CO}:\text{CO}_2$  ratios  $> 20$  ppb:ppm were flagged, which was 34 more days. We also filtered for Santa Ana wind events, characterized by unusually low variations throughout a day. Days with changes of  $X_{\text{CO}_2} < 0.8$  ppm or  $X_{\text{CH}_4} < 5$  ppb or  $X_{\text{CO}} < 2.5$  ppb were eliminated which was an additional 111 days. In total 18% of the total days were flagged by all filters. Of the 158 days with measurements at JPL, 37 were filtered by the Caltech flags. JPL data were flagged similarly to Caltech, except low outlier flag limits were set at 75% because we expect average enhancements to be less at JPL. This eliminated 20 more days for a total of 101 comparison days between Caltech and JPL.

AFRC is considered a background site and there are 514 comparison days with Caltech that are not filtered by the Caltech flags (of 640 days through June 2016). Days with changes of  $X_{\text{CO}_2} > 2.0$  ppm or  $X_{\text{CH}_4} > 23$  ppb or  $X_{\text{CO}} > 15$  ppb were eliminated, which was an additional 42 days, for a total of 472 comparison days between Caltech and AFRC.

## References

- Affek, H. P., X. Xu, and J. M. Eiler (2007), Seasonal and diurnal variations of  $^{13}\text{C}^{18}\text{O}^{16}\text{O}$  in air: Initial observations from Pasadena, CA, *Geochim. Cosmochim. Acta*, *71*, 5033–5043, doi:10.1016/j.gca.2007.08.014.
- Brioude, J., et al. (2013), Top-down estimate of surface flux in the Los Angeles Basin using a mesoscale inverse modeling technique: Assessing anthropogenic emissions of  $\text{CO}$ ,  $\text{NO}_x$  and  $\text{CO}_2$  and their impacts, *Atmos. Chem. Phys.*, *13*, 3661–3677, doi:10.5194/acp-13-3661-2013.

### Acknowledgments

ASTER GDEM is a product of METI and NASA. We gratefully acknowledge the NOAA Air Resources Laboratory (ARL) for the provision of the HYSPLIT transport and dispersion model (<http://www.ready.noaa.gov>) used in this publication. OCO-2 lite files were produced by the OCO-2 project at the Jet Propulsion Laboratory, California Institute of Technology, and obtained from the OCO-2 data archive maintained at the NASA Goddard Earth Science Data and Information Services Center. Nightlight products were obtained from the Earth Observation Group, NOAA National Geophysical Data Center and are based on Suomi NPP satellite observations (<http://ngdc.noaa.gov/eog/viirs/>). TCCON data are available from the CDIAC and will also be available through the Caltech library archive by 2018 [*Iraci et al.*, 2014; *Wennberg et al.*, 2014b, 2014a]. Model data are available upon request. We thank Chris O'Dell and the ACOS team for early access to the GOSAT-ACOS v7.3 data. We thank Camille Viatte, Eric Kort, and Kristal Verhulst for helpful discussions. The authors thank funding sources. This work is supported in part by the W. M. Keck Institute for Space Studies. The authors gratefully acknowledge TCCON funding from the NASA Carbon Cycle Science program (grant numbers NNX14AI60G and NNX17AE15G), and the Jet Propulsion Laboratory OCO-2 program (grant 1517180). Kevin R. Gurney thanks NIST grant 70NANB14H321. The authors also wish to thank the OCO-2 Science Team grant NNX15AI42G and NASA EVS ACT-America grant NNX15AG76G. The authors thank the referees for their comments. This paper is edited by A. Steiner and reviewed by two anonymous referees.

- Chen, J., C. Viatte, J. K. Hedelius, T. Jones, J. E. Franklin, H. Parker, E. W. Gottlieb, P. O. Wennberg, M. K. Dubey, and S. C. Wofsy (2016), Differential column measurements using compact solar-tracking spectrometers, *Atmos. Chem. Phys.*, *16*, 8479–8498, doi:10.5194/acp-16-8479-2016.
- Crisp, D., et al. (2012), The ACOS CO<sub>2</sub> retrieval algorithm—Part II: Global X<sub>CO<sub>2</sub></sub> data characterization, *Atmos. Meas. Tech.*, *5*, 687–707, doi:10.5194/amt-5-687-2012.
- Djuricin, S., D. E. Pataki, and X. Xu (2010), A comparison of tracer methods for quantifying CO<sub>2</sub> sources in an urban region, *J. Geophys. Res.*, *115*, D11303, doi:10.1029/2009JD012236.
- Duren, R. M., and C. E. Miller (2012), Measuring the carbon emissions of megacities, *Nat. Clim. Change*, *2*, 560–562, doi:10.1038/nclimate1629.
- Eldering, A., et al. (2017), The Orbiting Carbon Observatory-2: First 18 months of science data products, *Atmos. Meas. Tech.*, *10*, 549–563, doi:10.5194/amt-10-549-2017.
- Etheridge, D., L. Steele, R. Langenfelds, R. Rancey, J.-M. Barnola, and V. Morgan (1996), Natural and anthropogenic changes in atmospheric CO<sub>2</sub> over the last 1000 years from air in Antarctic ice and firn, *J. Geophys. Res.*, *101*, 4115–4128, doi:10.1029/95JD03410.
- Feldman, D. R., W. D. Collins, P. J. Gero, M. S. Torn, E. J. Mlawer, and T. R. Shippert (2015), Observational determination of surface radiative forcing by CO<sub>2</sub> from 2000 to 2010, *Nature*, *519*, 339–343, doi:10.1038/nature14240.
- Feng, S., et al. (2016), LA megacity: A high-resolution land-atmosphere modelling system for Urban CO<sub>2</sub> emissions, *Atmos. Chem. Phys.*, *16*, 9019–9045, doi:10.5194/acp-2016-143.
- Gurney, K. R., I. Razlivanow, Y. Song, Y. Zhou, B. Bedrich, and M. Abdul-massih (2012), Quantification of fossil fuel CO<sub>2</sub> emissions on the building/street scale for a large U.S. City, *Environ. Sci. Technol.*, *46*, 12 194–12,202, doi:10.1021/es3011282.
- Hanemann, M., S. de la Rue du Can, T. Wenzel, and L. Price (2008), *Improving the Carbon Dioxide Emission Estimates from the Combustion of Fossil Fuels in California and Spatial Disaggregated Estimate of Energy-related Carbon Dioxide for California*. [Available at <http://www.arb.ca.gov/research/apr/past/05-310.pdf>].
- Hase, F., M. Frey, T. Blumenstock, J. Groß, M. Kiel, R. Kohlhepp, G. Mengistu Tsidu, K. Schäfer, M. K. Sha, and J. Orphal (2015), Application of portable FTIR spectrometers for detecting greenhouse gas emissions of the major city Berlin, *Atmos. Meas. Tech.*, *8*, 3059–3068, doi:10.5194/amt-8-3059-2015.
- Hedelius, J. K., et al. (2017), Intercomparability of X<sub>CO<sub>2</sub></sub> and X<sub>CH<sub>4</sub></sub> from the United States TCCON sites, *Atmos. Meas. Tech.*, *10*, 1481–1493, doi:10.5194/amt-10-1481-2017.
- Hersey, S. P., et al. (2013), Composition and hygroscopicity of the Los Angeles Aerosol CalNex, *J. Geophys. Res. Atmos.*, *118*, 3016–3036, doi:10.1002/jgrd.50307.
- Hoornweg, D., L. Sugar, M. Freire, C. Anderson, B. Perinaz, C. L. Trejos, R. Dave, M. Lee, A. Joshi-Ghani, and Z. Allaoua (2010), *Cities and Climate Change: An Urgent Agenda*, World Bank, Washington, D. C. [Available at <http://siteresources.worldbank.org/INTUWM/Resources/340232-1205330656272/CitiesandClimateChange.pdf>].
- Iraci, L., et al. (2014), TCCON data from Armstrong Flight Research Center, Edwards, CA, USA, Release GGG2014R1, doi:10.14291/tcon.ggg2014.edwards01.R1/1255068.
- Janardan, R., S. Maksyutov, T. Oda, M. Saito, J. W. Kaiser, A. Ganshin, A. Stohl, T. Matsunaga, Y. Yoshida, and T. Yokota (2016), Comparing GOSAT observations of localized CO<sub>2</sub> enhancements by large emitters with inventory-based estimates, *Geophys. Res. Lett.*, *43*, 3486–3493, doi:10.1002/2016GL067843.
- Keppel-Aleks, G., P. O. Wennberg, C. W. O'Dell, and D. Wunch (2013), Towards constraints on fossil fuel emissions from total column carbon dioxide, *Atmos. Chem. Phys.*, *13*, 4349–4357, doi:10.5194/acp-13-4349-2013.
- Kort, E. A., C. Frankenberg, C. E. Miller, and T. Oda (2012), Space-based observations of megacity carbon dioxide, *Geophys. Res. Lett.*, *39*, L17806, doi:10.1029/2012GL052738.
- Kort, E. A., W. M. Angevine, R. Duren, and C. E. Miller (2013), Surface observations for monitoring urban fossil fuel CO<sub>2</sub> emissions: Minimum site location requirements for the Los Angeles megacity, *J. Geophys. Res. Atmos.*, *118*, 1577–1584, doi:10.1002/jgrd.50135.
- Kuze, A., H. Suto, M. Nakajima, and T. Hamazaki (2009), Thermal and near infrared sensor for carbon observation Fourier-transform spectrometer on the Greenhouse Gases Observing Satellite for greenhouse gases monitoring, *Appl. Opt.*, *48*, 6716–6733, doi:10.1364/AO.48.006716.
- Kuze, A., et al. (2016), Update on GOSAT TANSO-FTS performance, operations, and data products after more than six years in space, *Atmos. Meas. Tech.*, *9*, 2445–2461, doi:10.5194/amt-9-2445-2016.
- Mandrake, L., and G. Doran (2015a), Warn levels: Ordering data for custom filtration in 11th International Workshop on Greenhouse Gas Measurements from Space, paper presented at 11th International Workshop on Greenhouse Gas Measurements from Space, Pasadena, Calif. [Available at <https://drive.google.com/file/d/0BxA3HC2mAmDha1FfN2pfQ2JtcXc/view>].
- Mandrake, L., and G. Doran (2015b), DOGO warn levels: You've got them, let's use them, paper presented at OCO-2 second Post-Launch OCO-2 Science Team Meeting, Pasadena, Calif. [Available at [http://ml.jpl.nasa.gov/papers/mandrake/mandrake\\_2015\\_WL.pdf](http://ml.jpl.nasa.gov/papers/mandrake/mandrake_2015_WL.pdf)].
- McKain, K., S. C. Wofsy, T. Nehrkorn, J. Eluszkiewicz, J. R. Ehleringer, and B. B. Stephens (2012), Assessment of ground-based atmospheric observations for verification of greenhouse gas emissions from an urban region, *Proc. Natl. Acad. Sci. U. S. A.*, *109*, 8423–8428, doi:10.1073/pnas.1116645109.
- Myhre, G., et al. (2013), Anthropogenic and natural radiative forcing, in *Climate Change 2013: The Physical Science Basis. Contribution of Working Group I to the Fifth Assessment Report of the Intergovernmental Panel on Climate Change*, edited by T. F. Stocker et al., pp. 659–740, Cambridge Univ. Press, Cambridge, U. K., and New York, doi:10.1017/CBO9781107415324.018.
- Newman, S., X. Xu, H. P. Affek, E. Stolper, and S. Epstein (2008), Changes in mixing ratio and isotopic composition of CO<sub>2</sub> in urban air from the Los Angeles basin, California, between 1972 and 2003, *J. Geophys. Res.*, *113*, D23304, doi:10.1029/2008JD009999.
- Newman, S., et al. (2013), Diurnal tracking of anthropogenic CO<sub>2</sub> emissions in the Los Angeles basin megacity during spring 2010, *Atmos. Chem. Phys.*, *13*, 4359–4372, doi:10.5194/acp-13-4359-2013.
- Newman, S., et al. (2016), Toward consistency between trends in bottom-up CO<sub>2</sub> emissions and top-down atmospheric measurements in the Los Angeles megacity, *Atmos. Chem. Phys.*, *16*, 3843–3863, doi:10.5194/acp-16-3843-2016.
- Nielsen-Gammon, J. W., C. L. Powell, M. J. Mahoney, W. M. Angevine, C. Senff, A. White, C. Berkowitz, C. Doran, and K. Knupp (2008), Multisensor estimation of mixing heights over a coastal city, *J. Appl. Meteorol. Climatol.*, *47*, 27–43, doi:10.1175/2007JAMC1503.1.
- O'Dell, C. W., et al. (2012), The ACOS CO<sub>2</sub> retrieval algorithm—Part I: Description and validation against synthetic observations, *Atmos. Meas. Tech.*, *5*, 99–121, doi:10.5194/amt-5-99-2012.
- Pavley, F., and F. Nunez (2006), California Assembly Bill No. 32-Global Warming Solutions Act of 2006. [Available at <http://www.arb.ca.gov/cc/docs/ab32text.pdf>].
- Perry, S. G., and W. H. Snyder (2017), Laboratory simulations of the atmospheric mixed-layer in flow over complex topography, *Phys. Fluids*, *29*, 020702, doi:10.1063/1.4974505.

- Schneider, A., M. A. Friedl, and D. Potere (2009), A new map of global urban extent from MODIS satellite data, *Environ. Res. Lett.*, *4*, 044003, doi:10.1088/1748-9326/4/4/044003.
- Seto, K. C., et al. (2014), Human settlements, infrastructure, and spatial planning, in *Climate Change 2014: Mitigation of Climate Change. Contribution of Working Group III to the Fifth Assessment Report of the Intergovernmental Panel on Climate Change*, edited by O. Edenhofer et al., pp. 923–1000, Cambridge Univ. Press, Cambridge, U. K., and New York, doi:10.1017/CBO9781107415416.018.
- Shultz, P., and T. T. Warner (1981), Characteristics of summertime circulations and pollutant ventilation in the Los Angeles Basin.pdf, *J. Appl. Meteorol.*, *21*, 672–682, doi:10.1175/1520-0450(1982)021<0672:COSSCAP>2.0.CO;2.
- United Nations (2014), *World Urbanization Prospects, The 2014 Revision: Highlights*, U. N. Dep. of Econ. and Soc. Affairs, New York.
- Verhulst, K. R., et al. (2016), Carbon dioxide and methane measurements from the Los Angeles Megacity Carbon Project: 1. Calibration, urban enhancements, and uncertainty estimates, *Atmos. Chem. Phys. Discuss*, doi:10.5194/acp-2016-850.
- Villaraigosa, A. R. (2007), Green LA: An action plan to lead the nation in fighting global warming. [Available at [http://www.ci.la.ca.us/mayor/villaraigosaplan/EnergyandEnvironment/LACITY\\_004467.htm](http://www.ci.la.ca.us/mayor/villaraigosaplan/EnergyandEnvironment/LACITY_004467.htm).]
- Ware, J., E. A. Kort, P. DeCola, and R. Duren (2016), Aerosol lidar observations of atmospheric mixing in Los Angeles: Climatology and implications for greenhouse gas observations, *J. Geophys. Res. Atmos.*, *121*, 9862–9878, doi:10.1002/2016JD024953.
- Wehr, R., J. W. Munger, J. B. McManus, D. D. Nelson, M. S. Zahniser, E. A. Davidson, S. C. Wofsy, and S. R. Saleska (2016), Seasonality of temperate forest photosynthesis and daytime respiration, *Nature*, *534*, 680–683, doi:10.1038/nature17966.
- Wennberg, P. O., C. Roehl, J.-F. Blavier, D. Wunch, J. Landeros, and N. Allen (2014a), *TCCON data from Jet Propulsion Laboratory*, Release GGG2014R0. TCCON data archive, Pasadena, Calif.
- Wennberg, P. O., D. Wunch, C. Roehl, J.-F. Blavier, G. C. Toon, and N. Allen (2014b), *TCCON data from California Institute of Technology*, Release GGG2014R0. TCCON data archive, Pasadena, Calif.
- Worden, J., G. Doran, S. Kulawik, A. Eldering, D. Crisp, C. Frankenberg, C. O'Dell, and K. Bowman (2016), Evaluation And Attribution Of OCO-2 XCO<sub>2</sub> Uncertainties, *Atmos. Meas. Tech. Discuss*, doi:10.5194/amt-2016-175.
- Wunch, D., P. O. Wennberg, G. C. Toon, G. Keppel-Aleks, and Y. G. Yavin (2009), Emissions of greenhouse gases from a North American megacity, *Geophys. Res. Lett.*, *36*, L15810, doi:10.1029/2009GL039825.
- Wunch, D., et al. (2010), Calibration of the Total Carbon Column Observing Network using aircraft profile data, *Atmos. Meas. Tech.*, *3*, 1351–1362, doi:10.5194/amt-3-1351-2010.
- Wunch, D., G. C. Toon, J.-F. L. Blavier, R. A. Washenfelder, J. Notholt, B. J. Connor, D. W. T. Griffith, V. Sherlock, and P. O. Wennberg (2011), The total carbon column observing network, *Philos. Trans. R. Soc. London, Ser. A*, *369*, 2087–2112, doi:10.1098/rsta.2010.0240.
- Wunch, D., G. C. Toon, V. Sherlock, N. M. Deutscher, C. Liu, D. G. Feist, and P. O. Wennberg (2015), *The Total Carbon Column Observing Network's GGG2014 Data Version*, 43 pp., Carbon Dioxide Inf. Anal. Cent., Oak Ridge Natl. Lab., Oak Ridge, Tenn.
- Wunch, D., G. C. Toon, J. K. Hedelius, N. Vizenor, C. M. Roehl, K. M. Saad, J.-F. L. Blavier, D. R. Blake, and P. O. Wennberg (2016), Quantifying the loss of processed natural gas within California's South Coast Air Basin using long-term measurements of ethane and methane, *Atmos. Chem. Phys.*, *16*, 14091–14105, doi:10.5194/acp-16-14091-2016.
- Wunch, D., et al. (2017), Comparisons of the Orbiting Carbon Observatory-2 (OCO-2) XCO<sub>2</sub> measurements with TCCON, *Atmos. Meas. Tech.*, *10*, 2209–2238, doi:10.5194/amt-10-2209-2017.
- Yang, Z., R. A. Washenfelder, G. Keppel-Aleks, N. Y. Krakauer, J. T. Randerson, P. P. Tans, C. Sweeney, and P. O. Wennberg (2007), New constraints on Northern Hemisphere growing season net flux, *Geophys. Res. Lett.*, *34*, L12807, doi:10.1029/2007GL029742.